Regular Article - Experimental Physics

Two-particle correlations in azimuthal angle and pseudorapidity in central ^{7}Be + ^{9}Be collisions at the CERN Super Proton Synchrotron

NA61/SHINE Collaboration

A. Aduszkiewicz[15], E. V. Andronov[21], T. Antićić[3], V. Babkin[19], M. Baszczyk[13], S. Bhosale[10], A. Blondel[4], M. Bogomilov[2], A. Brandin[20], A. Bravar[23], W. Bryliński[17], J. Brzychczyk[12], M. Buryakov[19], O. Busygina[18], A. Bzdak[13], H. Cherif[6], M. Ćirković[22], M. Csanad[7], J. Cybowska[17], T. Czopowicz[9,17], A. Damyanova[23], N. Davis[10], M. Deliyergiyev[9], M. Deveaux[6], A. Dmitriev[19], W. Dominik[15], P. Dorosz[13], J. Dumarchez[4], R. Engel[5], G. A. Feofilov[21], L. Fields[24], Z. Fodor[7,16], A. Garibov[1], M. Gaździcki[6,9], O. Golosov[20], V. Golovatyuk[19], M. Golubeva[18], K. Grebieszkow[17], F. Guber[18], A. Haesler[23], S. N. Igolkin[21], S. Ilieva[2], A. Ivashkin[18], S. R. Johnson[25], K. Kadija[3], N. Kargin[20], E. Kashirin[20], M. Kiełbowicz[10], V. A. Kireyeu[19], V. Klochkov[6], V. I. Kolesnikov[19], D. Kolev[2], A. Korzenev[23], V. N. Kovalenko[21], S. Kowalski[14], M. Koziel[6], A. Krasnoperov[19], W. Kucewicz[13], M. Kuich[15], A. Kurepin[18], D. Larsen[12], T. V. Lazareva[21], M. Lewicki[16], K. Łojek[12], V. V. Lyubushkin[19], M. Maćkowiak-Pawłowska[17], Z. Majka[12], B. Maksiak[11,a] , A. I. Malakhov[19], A. Marcinek[10], A. D. Marino[25], K. Marton[7], H.-J. Mathes[5], T. Matulewicz[15], V. Matveev[19], G. L. Melkumov[19], A. O. Merzlaya[12], B. Messerly[26], Ł. Mik[13], S. Morozov[18,20], S. Mrówczyński[9], Y. Nagai[25], M. Naskręt[16], V. Ozvenchuk[10], V. Paolone[26], O. Petukhov[18], R. Płaneta[12], P. Podlaski[15], B. A. Popov[4,19], B. Porfy[7], M. Posiadała-Zezula[15], D. S. Prokhorova[21], D. Pszczel[11], S. Puławski[14], J. Puzović[22], M. Ravonel[23], R. Renfordt[6], D. Röhrich[8], E. Rondio[11], M. Roth[5], B. T. Rumberger[25], M. Rumyantsev[19], A. Rustamov[1,6], M. Rybczynski[9], A. Rybicki[10], A. Sadovsky[18], K. Schmidt[14], I. Selyuzhenkov[20], A. Yu. Seryakov[21], P. Seyboth[9], M. Słodkowski[17], P. Staszel[12], G. Stefanek[9], J. Stepaniak[11], M. Strikhanov[20], H. Ströbele[6], T. Šuša[3], A. Taranenko[20], A. Tefelska[17], D. Tefelski[17], V. Tereshchenko[19], A. Toia[6], R. Tsenov[2], L. Turko[16], R. Ulrich[5], M. Unger[5], D. Uzhva[21], F. F. Valiev[21], D. Veberič[5], V. V. Vechernin[21], A. Wickremasinghe[24,26], Z. Włodarczyk[9], K. Wojcik[14], O. Wyszyński[9], E. D. Zimmerman[25], R. Zwaska[24]

1 National Nuclear Research Center, Baku, Azerbaijan
2 Faculty of Physics, University of Sofia, Sofia, Bulgaria
3 Ruđer Bošković Institute, Zagreb, Croatia
4 LPNHE, University of Paris VI and VII, Paris, France
5 Karlsruhe Institute of Technology, Karlsruhe, Germany
6 University of Frankfurt, Frankfurt, Germany
7 Wigner Research Centre for Physics of the Hungarian Academy of Sciences, Budapest, Hungary
8 University of Bergen, Bergen, Norway
9 Jan Kochanowski University in Kielce, Kielce, Poland
10 Institute of Nuclear Physics, Polish Academy of Sciences, Kraków, Poland
11 National Centre for Nuclear Research, Warsaw, Poland
12 Jagiellonian University, Kraków, Poland
13 AGH-University of Science and Technology, Kraków, Poland
14 University of Silesia, Katowice, Poland
15 University of Warsaw, Warsaw, Poland
16 University of Wrocław, Wrocław, Poland
17 Warsaw University of Technology, Warsaw, Poland
18 Institute for Nuclear Research, Moscow, Russia
19 Joint Institute for Nuclear Research, Dubna, Russia
20 National Research Nuclear University (Moscow Engineering Physics Institute), Moscow, Russia
21 St. Petersburg State University, St. Petersburg, Russia
22 University of Belgrade, Belgrade, Serbia
23 University of Geneva, Geneva, Switzerland
24 Fermilab, Batavia, USA
25 University of Colorado, Boulder, USA
26 University of Pittsburgh, Pittsburgh, USA

a e-mail: Bartosz.Maksiak@ncbj.gov.pl

Abstract A measurement of charged hadron pair correlations in two-dimensional $\Delta\eta\Delta\phi$ space is presented. The analysis is based on total 30 million central Be + Be collisions observed in the NA61/SHINE detector at the CERN SPS for incident beam momenta of $19A$, $30A$, $40A$, $75A$, and $150A$ GeV/c. Measurements were carried out for unlike-sign and like-sign charge hadron pairs independently. The $C(\Delta\eta, \Delta\phi)$ correlation functions were compared with results from a similar analysis on p + p interactions at similar beam momenta per nucleon. General trends of the back-to-back correlations are similar in central Be + Be collisions and p + p interactions, but are suppressed in magnitude due to the increased combinatorial background. Predictions from the Epos and UrQMD models are compared to the measurements. Evolution of an enhancement around $(\Delta\eta, \Delta\phi) = (0, 0)$ with incident energy is observed in central Be + Be collisions. It is not predicted by both models and almost non-existing in proton–proton collisions at the same momentum per nucleon.

1 Introduction and motivation

This paper presents experimental results on two-particle correlations in pseudorapidity and azimuthal angle of charged particles produced in central Be + Be collisions at $19A$, $30A$, $40A$, $75A$, and $150A$ GeV/c. The measurements were performed by the multi-purpose NA61/SHINE [1] experiment at the CERN Super Proton Synchrotron (SPS). They are part of the strong interactions programme devoted to the study of the properties of the onset of deconfinement and search for the critical point of strongly interacting matter. Within this program a two-dimensional scan in collision energy and size of colliding nuclei recorded data on p + p, Be + Be, Ar + Sc, Xe + La, and Pb + Pb collisions and was completed in 2018. The expected signal of a critical point is a non-monotonic dependence of various fluctuation measures in such a scan; for a recent review see Ref. [2].

Apart from looking for critical point (CP) and quark-gluon plasma (QGP) signatures, it is of interest to study specific physical phenomena that happen during and after the collision. The two-particle correlation analysis in pseudorapidity (η) and azimuthal angle (ϕ) allows to disentangle different correlation sources which may be directly connected with phenomena like jets, collective flow, resonance decays, quantum statistics effects, conservation laws, etc.

Measurements of two-particle correlations in pseudorapidity and azimuthal angle were first published by the ACM collaboration at the Intersecting Storage Rings (ISR) [3]. Two- and three-body decays of resonances (η, ρ^0, ω) were found to provide the dominant contributions. Two structures were observed: an enhancement near $\Delta\phi = \pi$ (away-side) explained by the two-body decay scenario and another enhancement at $\Delta\phi \approx 0$ together with an azimuthal ridge (centered at $\Delta\eta \approx 0$) consistent with three-body decays.[1] These features were confirmed at the higher collision energies of Relativistic Heavy Ion Collider (RHIC) by the PHO-BOS [4] collaboration.

At RHIC and the Large Hadron Collider (LHC) parton scattering processes become important. In addition to high transverse momentum jets, studies of $\Delta\eta\Delta\phi$ correlations in p + p interactions as well as in collisions of heavy nuclei [5–8] found prominent structures explained as arising from the production of minijets, creating a large correlation peak at small opening angles ($\Delta\eta, \Delta\phi) \approx (0, 0)$ and a broad structure along $\Delta\eta$ at $\Delta\phi \approx \pi$ (also referred to as away-side ridge).

A study of two-particle correlations was already performed by NA61/SHINE in inelastic p + p interactions at SPS energies and reported in Ref. [9]. The results show structures connected most probably to resonance decays, momentum conservation, and Bose–Einstein correlations. No clear sign of jet-like structure was observed (a more detailed search for jet-like structures was performed in Ref. [10]).

This paper reports NA61/SHINE results from the next step in size of the collision system of two-particle correlations in $\Delta\eta$ and $\Delta\phi$ for the 5% most central ^{7}Be + ^{9}Be collisions. The data were recorded in 2011, 2012 and 2013 using a secondary ^{7}Be beam produced by fragmentation of the primary Pb beam from the CERN SPS [11]. The ^{7}Be + ^{9}Be collisions play a special role in the NA61/SHINE scan programme. The collision system composed of a ^{7}Be and a ^{9}Be nucleus has eight protons and eight neutrons, and thus is isospin symmetric. Within the NA61/SHINE scan programme the ^{7}Be + ^{9}Be collisions serve as the lowest mass isospin symmetric reference needed to study collisions of medium and large mass nuclei. This is of particular importance when data on proton–proton, neutron–proton and neutron–neutron are not available to construct the nucleon–nucleon reference [12]. Finally, the latest RHIC and LHC results suggest that collective effects may also be developed in small (p + Pb, d + Au) or high-multiplicity p + p systems (Refs. [13–15]).

Study of energy evolution of the near-side $\Delta\eta$, $\Delta\phi$ correlation in Be + Be is also of interest from the point of view of possible formation and decays of small QGP hotspots (Refs. [16–18]) because the products of the first stage of the interaction will undergo less scattering in surrounding matter than in the case of heavy nucleus–nucleus reactions.

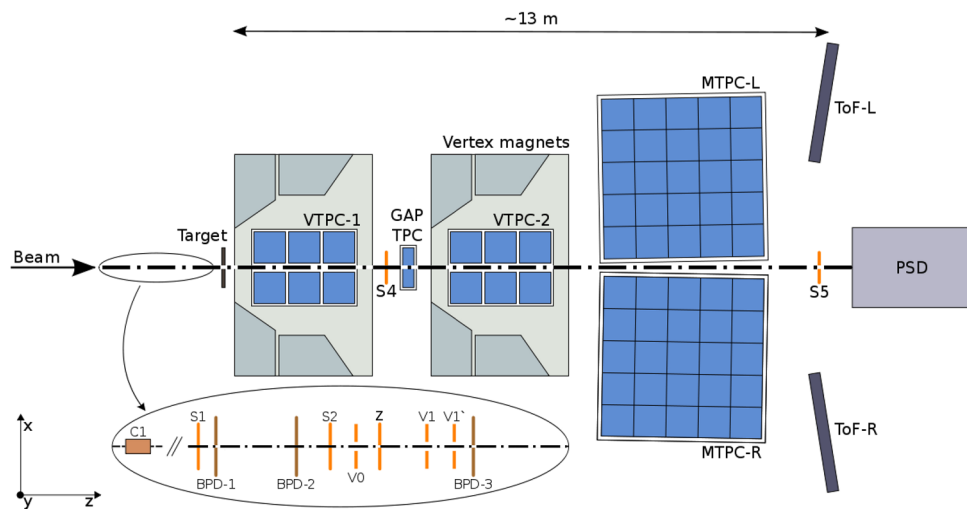[1] $\Delta\eta$ and $\Delta\phi$ definitions are in Eq. 1.

Fig. 1 The schematic layout of the NA61/SHINE experiment at the CERN SPS [1] showing the components used for the Be + Be energy scan (horizontal cut, not to scale). The beam instrumentation is sketched in the inset. Alignment of the chosen coordinate system as shown in the figure; its origin lies in the middle of VTPC-2, on the beam axis. The nominal beam direction is along the z axis. The magnetic field bends charged particle trajectories in the x–z (horizontal) plane. The drift direction in the TPCs is along the y (vertical) axis

In this paper the pseudorapidity variable η is calculated as $\eta = -\ln(\tan(\Theta/2))$, where $\tan(\Theta) = p_T/p_L$ with p_T the transverse (x, y) and p_L the longitudinal (z) component of the particle momentum in the collision centre-of-mass system. The pion mass was assumed for all particles in the Lorentz transformation of p_L measured in the laboratory system to the centre-of-mass system. The azimuthal angle ϕ is the angle between the transverse momentum vector and the horizontal (x) axis.

2 Two-particle correlations in pseudorapidity and azimuthal angle

Correlations studied in this paper were calculated as a function of the difference in pseudorapidity (η) and azimuthal angle (ϕ) between two particles produced in the same event:

$$\Delta\eta = |\eta_1 - \eta_2|, \quad \Delta\phi = |\phi_1 - \phi_2|. \tag{1}$$

The correlation function $C(\Delta\eta, \Delta\phi)$ is defined and calculated as:

$$C(\Delta\eta, \Delta\phi) = \frac{N_{\text{mixed}}^{\text{pairs}}}{N_{\text{data}}^{\text{pairs}}} \frac{D(\Delta\eta, \Delta\phi)}{M(\Delta\eta, \Delta\phi)}, \tag{2}$$

where

$$D(\Delta\eta, \Delta\phi) = \frac{d^2 N_{\text{data}}}{d\Delta\eta\, d\Delta\phi}, \quad M(\Delta\eta, \Delta\phi) = \frac{d^2 N_{\text{mixed}}}{d\Delta\eta\, d\Delta\phi}$$

are the distributions of particle pairs from the same (data) and from different (mixed) events, respectively. Distributions $D(\Delta\eta, \Delta\phi)$ and $M(\Delta\eta, \Delta\phi)$ were obtained by accumulating the number of pairs in intervals of $\Delta\eta$ and $\Delta\phi$. For the calculation of $C(\Delta\eta, \Delta\phi)$ both distributions were normalised to the number of pairs ($N_{\text{data}}^{\text{pairs}}$, $N_{\text{mixed}}^{\text{pairs}}$) in the given distribution.

The uncorrelated background was constructed by mixing particles from different data events with two main constraints: (a) the multiplicity distribution of mixed events had to be exactly the same as the original data event; (b) mixed events could not contain two particles from the same data event. The same method of mixing events was used in Ref. [9].

As stated in Eq. 1, the $\Delta\eta$ and $\Delta\phi$ values will get only positive values. Hence, the measurements were restricted to $0 \leq \Delta\eta \leq 3$ and $0 \leq \Delta\phi < \pi$. However, in order to better show the correlation structure, the results were mirrored along $\Delta\eta = 0$ and, assuming the periodicity in the range of 2π, also along $\Delta\phi = 0$ and $\Delta\phi = \pi$. Then, the distributions were shifted to the range $-\frac{\pi}{2} < \Delta\phi < \frac{3\pi}{2}$. These modifications were done to better demonstrate the most interesting correlation structures as well as to make them easily comparable with results obtained by other experiments (e.g. from Refs. [19,20]).

In this paper, the correlation function $C(\Delta\eta, \Delta\phi)$ was obtained for charged hadrons produced in strong and electromagnetic processes in Be + Be interactions within the NA61/SHINE acceptance. The acceptance maps are available in Ref. [21].

3 Experimental setup

This section gives a brief description of the experimental setup used for recording Be + Be collisions.

3.1 Detector

The NA61/SHINE experiment is a multi-purpose facility designed to measure particle production in nucleus–nucleus, hadron–nucleus and proton–proton interactions [1]. The detector is situated at the CERN Super Proton Synchrotron (SPS) in the H2 beamline of the North experimental area. A schematic diagram of the setup is shown in Fig. 1. The main components of the produced particle detection system are four large volume Time Projection Chambers (TPC). Two of them, called Vertex TPCs (VTPC), are located downstream of the target inside superconducting magnets with maximum combined bending power of 9 Tm. The magnetic field was scaled down in proportion to the beam momentum in order to obtain similar phase space acceptance at all energies. The main TPCs (MTPC) and two walls of pixel Time-of-Flight (ToF-L/R) detectors are placed symmetrically to the beamline downstream of the magnets. The fifth small TPC (GAP TPC) is located between VTPC-1 and VTPC-2 directly on the beam line. The TPCs are filled with $Ar:CO_2$ gas mixtures in proportions 90:10 for the VTPCs and the GAP-TPC, and 95:5 for the MTPCs.

The Projectile Spectator Detector (PSD), which measures mainly the energy of projectile spectators, is positioned 20.5 m (16.7 m) downstream of the target and behind the MTPCs at $75A$ and $150A$ GeV/c ($19A$, $30A$, $40A$ GeV/c), centered in the transverse plane on the deflected position of the beam. The PSD allows to select the centrality (violence) of the collision by imposing an upper limit on the measured spectator energy. For more details see Sects. 3.5 and 3.6.

The beamline instrumentation is schematically depicted in Fig. 2. A set of scintillation counters as well as Beam Position Detectors (BPDs) upstream of the spectrometer provide timing reference, selection, identification and precise measurement of the position and direction of individual beam particles.

3.2 ^{9}Be target

The target was a plate of ^{9}Be of 12 mm thickness placed 75 cm upstream of front face of VTPC-1. Mass concentrations of impurities were measured at 0.3% resulting in an estimated increase of the produced pion multiplicity by less than 0.5% due the small admixture of heavier elements [22]. No correction was applied for this negligible contamination. Data were taken with target inserted (90% of all recorded events) and target removed (10% of all recorded events).

3.3 ^{7}Be beam

The beamline of NA61/SHINE is designed for obtaining high beam purity even with secondary ion beams. The beam instrumentation (see Fig. 2) consists of scintillator counters (S) used for triggering and beam particle identification, veto scintillation counters (V) with a hole in the middle for rejection of upstream interactions and beam halo particles, and a Cherenkov charge detector Z. Three Beam Position Detectors are used for determination of the charge of individual beam particles.

This paragraph provides a brief description of the ^{7}Be beam properties (see Ref. [11]). Primary Pb^{82+} ions extracted from the SPS were steered toward a 180 cm long beryllium fragmentation target placed 535 m upstream of the NA61/SHINE experiment. The result is a mixture of nuclear fragments consisting of nucleons not participating in inelastic collisions (spectators) with momentum per nucleon equal to the beam momentum per nucleon smeared by the Fermi motion momentum. The spectrometers of the beamline allow to select beam particles based on the particle rigidity: $B\rho = 3.33 \cdot p_{beam}/Z$, where $B\rho$ can be adjusted by setting the current on the dipole magnets of the spectrometer and p_{beam} is the momentum and Z the charge of the beam particle. Thus, the spectrometers select particles with the desired A/Z ratio. The charge spectrum measured by the Cherenkov Z detector for rigidity corresponding to ^{7}Be is shown in Fig. 3. A well separated peak for charge $Z = 4$ is visible and high purity ^{7}Be ions can be selected by a cut on the measured charge Z as indicated by the red shading in Fig. 3. At test beam of momentum of $13.9A$ GeV/c it was also possible to measure the time-of-flight of the beam particles. As demonstrated in Fig. 4 the selected fragments are high purity ^{7}Be.

3.4 Trigger

The schematic of the placement of the beam and trigger detectors is shown in Fig. 2. The trigger setup consists of a set of scintillation counters recording the presence of the beam particle (S1, S2), a set of veto scintillation counters with a hole used to reject beam particles passing far from the centre of the beamline (V0, V1), and a charge detector (Z). Beam particles were defined by the coincidence $T1 = S1 \cdot S2 \cdot \overline{V1} \cdot Z(Be)$ and $T1 = S1 \cdot \overline{V0} \cdot \overline{V1} \cdot \overline{V1'} \cdot Z(Be)$ for low and high momentum data taking respectively. For the low beam momenta an interaction trigger detector (S4) was used to check whether the beam particle changed charge after passing through the target. In addition, central collisions were selected by requiring an energy signal below a set threshold from the 16 central modules of the PSD (see Sect. 3.5 for details). The event trigger condition thus was $T2 = T1 \cdot \overline{S4} \cdot \overline{PSD}$ for $19A$ and $30A$ GeV/c and $T2 = T1 \cdot \overline{PSD}$ for $40A$, $75A$ and $150A$ GeV/c. The PSD threshold was set to retain from ≈ 70 to $\approx 40\%$ of
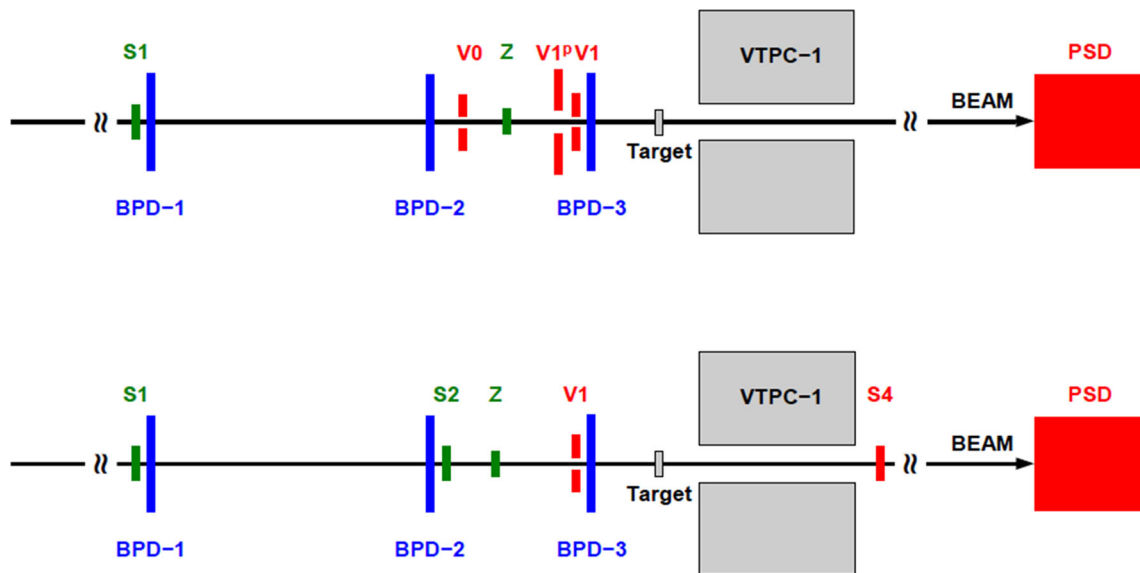
Fig. 2 The schematic of the placement of the beam and trigger detectors in high momentum (*top*) and low momentum (*bottom*) data taking
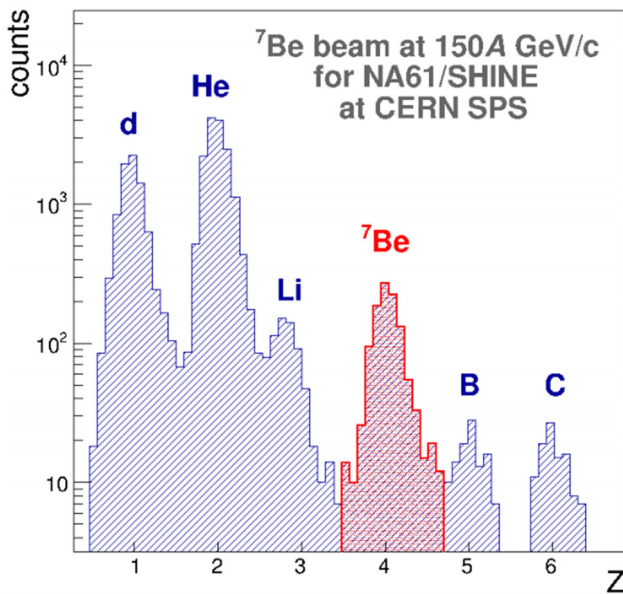

Fig. 3 Charge of the beam particles measured by the Z detector

inelastic collisions at beam momenta of 19*A* and 150*A* GeV/*c*, respectively.

3.5 The projectile spectator detector

The centrality measurement for the events used in this report is based on information from the Projectile Spectator Detector (PSD), which is a modular compensating zero-degree calorimeter. Thanks to its modularity, there is only small dependence of the measured energy on the position of the particle and there is the possibility to determine centrality based on the energy measured by a subset of modules.

The Projectile Spectator Detector used for this data taking consisted of 44 modules: 16 small (10×10 cm) modules in the central region of the detector and 28 large (20×20 cm) modules placed around the small modules. Each PSD module consisted of 60 pairs of alternating plates of lead and scintillator (Fig. 5, left). The signals from the scintillators of each module were read by 10 Silicon Photomultipliers (SiPMs). Each SiPM was connected through Wavelength Shifting (WLS) fibres to six consecutive scintillator plates in order to allow longitudinal calibration of the detector as well as the characterization of the longitudinal particle shower development.

The event trigger placed a cut on the summed signals of the 16 small central modules. In the offline analysis a subset of events was selected for which the summed energy from a larger group of modules (see Fig. 5 right) was required to lie below a threshold value in order to select the 5% most central collisions. The module choice was based on the existence of an anti-correlation between the recorded energy and the charged particle multiplicity reconstructed in the TPCs (a description of this method as well as an acceptance map for the region of the PSD used for centrality selection can be found in Ref. [23]). Moreover, the availability of these modules was required at all beam momenta.

3.6 Centrality determination

The determination of centrality (violence) in NA61/SHINE is based on the measurement of the energy deposited in the PSD by spectators (the most central collisions correspond to a low number of spectators and therefore a low energy deposit in the PSD). Only the central 16 modules are included in the
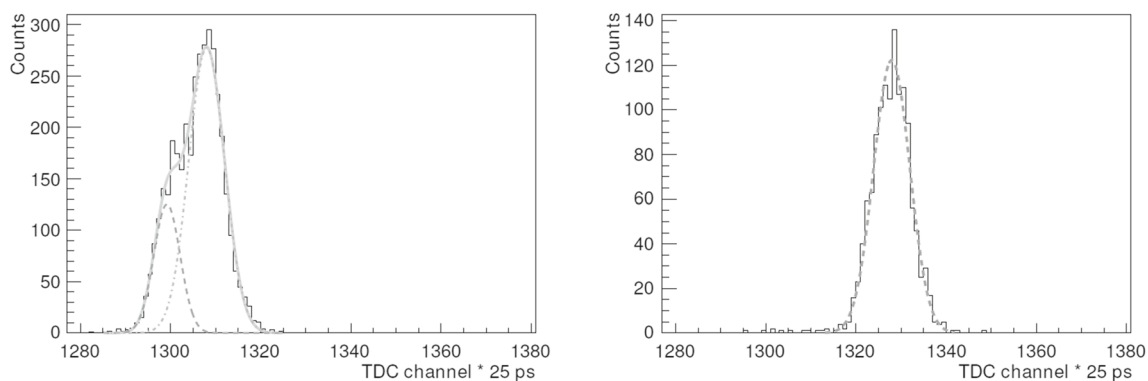
Fig. 4 Time-of-flight of fragments of Z/A with momentum of 13.9 GeV/c. Left: carbon ions shows double Gaussian structure due to two isotopes of carbon in the beam. Right: beryllium ions show single Gaussian distribution, indicating isotopic purity of the beryllium in the beam

Fig. 5 Left: construction schematic of a PSD module. Right: front face of the PSD showing modules in green used for centrality determination. The modules marked with gray colour were not installed yet during taking at 40A, 75A and 150A GeV/c
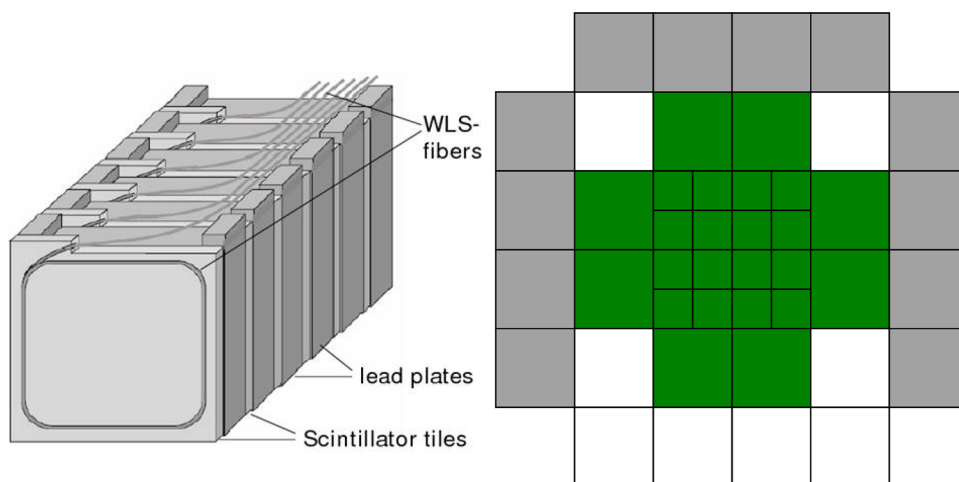
trigger. For offline analysis the energy recorded by a larger group of modules is summed (see Fig. 5).

4 Data processing, simulation and detector performance

Detector parameters were optimised by a data-based calibration procedure which also took into account their time dependence. Small adjustments were determined in consecutive steps for:

(i)   detector geometry, TPC drift velocities and distortions due to the magnetic field inhomogeneities in the corners of the VTPCs,
(ii) magnetic field setting,
(iii) specific energy loss measurements.

Each step involved the reconstruction of data required to optimise a given set of calibration constants and time dependent corrections followed by verification procedures. Details of the procedure and quality assessment are presented in Ref. [24]. The resulting performance relative to the mea-

surements of quantities relevant for this paper is discussed below.

The main steps of the data reconstruction procedure consists of: cluster finding in the TPC raw data, reconstruction of local track segments in each TPC separately, matching of local track segments and merging them into global tracks, track fitting based on a magnetic field map and determination of track parameters, determination of the interaction vertex using the beam information and the trajectories of tracks reconstructed in the TPCs, refitting of the particle trajectory using the interaction vertex as an additional point and determining the particle momentum vector at the interaction vertex.

A simulation of the NA61/SHINE detector response is used to correct the reconstructed data. For this purpose Be + Be collisions generated with the EPOS 1.99 [25,26] model were used to obtain the corrections for contamination by weak decays of strange particles, and reconstruction inefficiency of the NA61/SHINE detector.

The simulation consists of generating Be + Be collisions, propagating outgoing particles through the detector material using the GEANT 3.21 package [27], simulating the detector response using dedicated NA61/SHINE packages, sim-

Table 1 Number of events before and after cuts. See text for explanation of the columns

	Interactions	Good vertex	Vertex z pos.	Centrality 5%
19A GeV/c	565136	497624 (88%)	425346 (75%)	29531 (5%)
30A GeV/c	647662	592741 (92%)	513857 (79%)	38550 (6%)
40A GeV/c	1833013	881618 (48%)	776899 (42%)	109512 (6%)
75A GeV/c	2030413	927225 (46%)	822710 (41%)	92741 (5%)
150A GeV/c	1644127	833934 (51%)	732824 (45%)	81525 (5%)

ulating the interaction trigger selection, reconstructing the simulated events in the same way as the real data and matching reconstructed and simulated tracks based on the cluster positions (see Ref. [28] for more details).

5 Data selection and analysis

This section describes the procedure used for the analysis. It consists of the following steps: application of event and particle selections, obtaining uncorrected experimental results and evaluation of correction factors based on simulations, and finally calculation of statistical uncertainties and estimation of systematic uncertainties.

5.1 Event selection criteria

Due to the very small fraction of out-of-target interactions (less than one per mille) only interactions with target inserted were analysed, while target removed ones were not taken into account. The events selected for the analysis reported in this paper had to satisfy the following conditions:

(i) event was selected by the central interaction trigger[2] and was produced by a good quality[3] beam (Interactions).

(ii) event has a well-fitted main interaction vertex (Good vertex),

(iii) the maximal distance between the main vertex z position and the centre of the beryllium target is 2.5 cm (Vertex z pos.),

(iv) only the 5% most central collisions (based on PSD spectator energy measurement) are accepted (Centrality 5%).

Table 1 presents the number of events analysed for Be + Be reactions at five beam momenta.

5.2 Track selection criteria and acceptance

The tracks selected for the analysis had to satisfy the following conditions:

(i) the track fit of this charged particle converged (Good track),

(ii) the total number of reconstructed points on the track should be at least 30 and, at the same time, the sum of the number of reconstructed points in VTPC-1 and VTPC-2 should be at least 15 or the number of reconstructed points in the GAP TPC should be at least five (TPC nPoints),

(iii) the ratio of total number of reconstructed points (np) on the track to the potential number of points (nmp) should be between 0.5 and 1.2[4] (np/nmp).

(iv) the distance between the track extrapolated to the interaction plane and the interaction point (impact parameter) should be smaller or equal to 4 cm in the horizontal (bending – b_x) plane and 2 cm in the vertical (drift – b_y) plane[5] (b_x and b_y),

(v) tracks with dE/dx and total momentum values characteristic for electrons are rejected[6] (No e$^-$/e$^+$).

Numbers of tracks after consecutive selection cuts are presented in Table 2.

Model simulations were performed in 4π acceptance, thus the NA61/SHINE detector acceptance filter needed to be applied before comparisons with data. The detector acceptance was defined as a three-dimensional matrix (p,p_T,ϕ) filled with 1 or 0 depending on whether the bin was or was not populated by particles reconstructed and accepted in the events (see Ref. [21]).

For reconstructed tracks from simulation, the cut rejecting electrons and positrons was implemented differently. Due to the lack of information on simulated specific energy

---

[2] Central interaction trigger accepted approximately 40-50% minimum-bias events.

[3] Good quality of the beam was assured by: ensuring that beam was composed purely from beryllium ions, rejection of off-time interactions in the target, proper positioning of beam along BPDs.

[4] Due to uncertainty of the momentum fitting and the fitted interaction point, the np/nmp ratio values may exceed 1. Hence, the upper limit for the ratio was established as 1.2.

[5] Track impact point resolution depends on track multiplicity in the event as well as the method of vertex determination. Typically, it is at the level of 2 cm in x and 1 cm in y plane.

[6] See Ref. [29] for the details of this cut.

Table 2 Number of tracks before and after cuts for the 5% most central Be + Be collisions. See text for explanation of the columns

	Good track	TPC nPoints	np/nmp	b_x and b_y	No e$^-$/e$^+$
19A GeV/c	358504	257617 (72%)	234868 (66%)	227529 (63%)	215949 (60%)
30A GeV/c	605627	443356 (73%)	407537 (67%)	393572 (65%)	375621 (62%)
40A GeV/c	2009333	1499813 (75%)	1388029 (69%)	1338798 (67%)	1282954 (64%)
75A GeV/c	2413377	1823376 (76%)	1696029 (70%)	1640207 (68%)	1585880 (66%)
150A GeV/c	2943518	2185182 (74%)	2023686 (69%)	1962862 (67%)	1916593 (65%)

loss for reconstructed simulated tracks, a procedure called "matching" was introduced. It connects the currently examined reconstructed to the best matched simulated track candidate by comparing properties of simulated tracks before reconstruction with the properties of the simulated track after reconstruction. The selection of the best candidate is performed in two steps:

1. Pre-select the candidates that have a minimum value for the matching ratio A/B, where A is a number of points common for both simulated and reconstructed track and B is number of points for the simulated track. The matching of points between simulated and reconstructed tracks is based on the respective positions of the points,
2. From the preselected candidates, choose the one with the highest A value.

During the process of the analysis it was found that the minimal matching ratio value has an impact on the magnitude of the correlation in the region near $(\Delta\eta, \Delta\phi) = (0, 0)$. An analysis based on loss of accepted tracks versus increasing matching ratio value resulted in the choice of the optimal ratio of $A/B \geq 0.6$. The variation related to the choice of the minimal ratio was included in the systematic uncertainty (see Sect. 5.5).

5.3 Corrections

In order to correct the results for biases due to off-line event and track selection, detection efficiency, contribution of weak decays and secondary interaction products, an identical procedure was applied to the simulated data. The EPOS 1.99 model was used for event generation as it was done for inelastic p + p interactions [9]. Correction factors Corr($\Delta\eta, \Delta\phi$) were calculated bin-by-bin as the ratio of the correlation functions for simulated events ("pure") and for the same events after processing through GEANT 3.21 [27] detector simulation and reconstruction ("rec"), filtered using the same event and track selection cuts as for the data. The correlation function is derived from differences of extensive quantities of the two particles and is therefore not expected to be sensi-

tive to the details of the centrality selection. Thus a special correction is not required.

5.4 Statistical uncertainties

Statistical uncertainties of the correlation function are calculated in every $(\Delta\eta, \Delta\phi)$ bin using the following formula:

$$\sigma(C) = \sqrt{[\text{Corr} \cdot \sigma(C^{\text{raw}})]^2 + [C^{\text{raw}} \cdot \sigma(\text{Corr})]^2}, \qquad (3)$$

where C^{raw} is the uncorrected correlation function obtained following Eq. 2 and Corr($\Delta\eta, \Delta\phi$) is the correction factor (described in Sect. 5.3). Detailed evaluation of this formula is described in Sec. 4.3.1 in Ref. [10].

In general, statistical uncertainties do not exceed 5%. The highest uncertainties are for $\Delta\eta$ regions with lower statistics, i.e. for $\Delta\eta > 2$ and for positively and negatively charged pairs of particles and lower beam momenta. Below $\Delta\eta = 2$ statistical uncertainties are within 3% for beam momenta 19A, and 30A GeV and within 1.5% for 40A, 75A and 150A GeV.

5.5 Estimation of systematic uncertainties

In order to estimate systematic uncertainties, the data were analysed with loose and tight event and track selection cuts. By modifying cuts, one changes the magnitude of the corrections due to various biasing effects. If the simulation perfectly reproduces the data, corrected results should be independent of the cuts. A dependence on the selection criteria is due to imperfections of the simulation and is used as an estimate of the systematic uncertainty. For example, systematic uncertainty caused by weakly decaying particles is estimated by varying b_x and b_y cuts. The standard set of cut values, presented in Sects. 5.1 and 5.2 together with values of loose and tight cuts are tabulated in Table 3.

Results for both sets of cuts were subtracted bin-by-bin (loose–tight). Since the differences in all bins follow Gaussian distributions with mean close to 0, the systematic uncertainties were taken to be approximately equal to the standard deviation of the distribution. This procedure was performed for all charge combinations (all charge, unlike-sign, positively and negatively charge pairs) and for all beam momenta.

Table 3 Event (top) and track (bottom) selection cuts. The standard cuts (centre) are used to obtain the final results, whereas the loose (left) and tight (right) cuts are employed to estimate systematic uncertainties (see Sects. 5.1 and 5.2, respectively). The last row applies only to reconstructed tracks from simulation (MC^{rec})

	Loose	Standard	Tight
Event cuts			
Interactions	Applied		
Good vertex	Applied		
Vertex z pos.	± 10 cm	± 2.5 cm	± 1.25 cm
Centrality 5%	Applied		
Track cuts			
Good track	Applied		
Total TPC points	≥ 10	≥ 30	
VTPC (GAP TPC) points	$> 10(5)$	$\geq 15(5)$	$\geq 30(6)$
np/nmp	(0.5; 1.2)	(0.5; 1.2)	(0.7; 1.0)
$|b_x|$	≤ 6 cm	≤ 4 cm	≤ 0.8 cm
$|b_y|$	≤ 5 cm	≤ 2 cm	≤ 0.8 cm
e^-/e^+ cut	Applied		
Matching ratio (MC^{rec} only)	≥ 0.5	≥ 0.6	≥ 0.7

Mean systematic uncertainties were calculated for two sub-regions of $\Delta\eta$. For $0 \leq \Delta\eta < 2$ mean systematic uncertainties are at the level 0.5% for all charge combinations and beam momenta. For the region of $2 \leq \Delta\eta \leq 3$ the mean systematic uncertainties are higher and are up to 2% for negatively charged pairs of particles at $19A$ GeV/c. Statistical uncertainties were not taken into account during this analysis.

6 Results and discussion

This section presents the final two-particle correlation results together with their possible explanations.

6.1 Two-particle correlation function $C(\Delta\eta, \Delta\phi)$

The corrected correlation functions for all charge pair combinations (all charge pairs, unlike-sign pairs, positively and negatively charge pairs) are presented in Figs. 6, 7, 8 and 9, respectively. Their values span the range between 0.9 and 1.1. Vanishing two-particle correlations would result in $C = 1$.

Two-particle correlations in Be + Be collisions show the following features:

(i) A maximum at $(\Delta\eta, \Delta\phi) = (0, \pi)$ emerging most probably due to resonance decays and momentum conservation. The maximum is most prominent for lower beam momenta and decreases with increasing beam momentum down to almost $C = 1$ for $150A$ GeV/c for like-sign pairs. For unlike-sign pairs the maximum depends weakly on beam momentum. Comparing positive and negative charge pairs one can notice that in positive pairs the maximum is stronger. This may be explained by Δ^{++} resonance production and decay which contributes mostly to that correlation region. For negative

charge pairs the maximum is barely visible due to the very low number of resonances decaying into two negatively charged particles.

(ii) An enhancement at $(\Delta\eta, \Delta\phi) = (0, 0)$ likely due to a mix of different phenomena. It is rather broad (a $\Delta\phi$ bin corresponds here to $15° \approx 0.26$ rad). At small $\Delta\phi$ (smaller than about $6° \approx 0.1$ rad) it can be explained by a mixture of Quantum Statistic effects, Coulomb and final state interactions. A difference in height between positive and negative charge pairs is visible, namely in positive charge pairs the peak is significantly smaller than in negative charge pairs (especially for lower beam momenta). It is most probably due to the admixture of protons and an interplay between Bose–Einstein and Fermi–Dirac statistics. The HBT + Coulomb + FS correlations give a significant contribution to that region, however they probably do not explain all the excess. A more detailed discussion is provided in Sect. 7.1.1.

7 Comparison with p + p data and with model predictions

In this section two-particle correlation results presented in the previous section are compared with published NA61/SHINE results from p + p interactions [9] and to theoretical predictions of the EPOS 1.99 and UrQMD 3.4 [30,31] models.

7.1 Comparison with correlations in p + p reactions

This section presents a comparison of two-particle correlation measurements for the 5% most central Be + Be collisions to those in inelastic p + p interactions reported in Ref. [9]. Figure 10 shows an example comparison of results
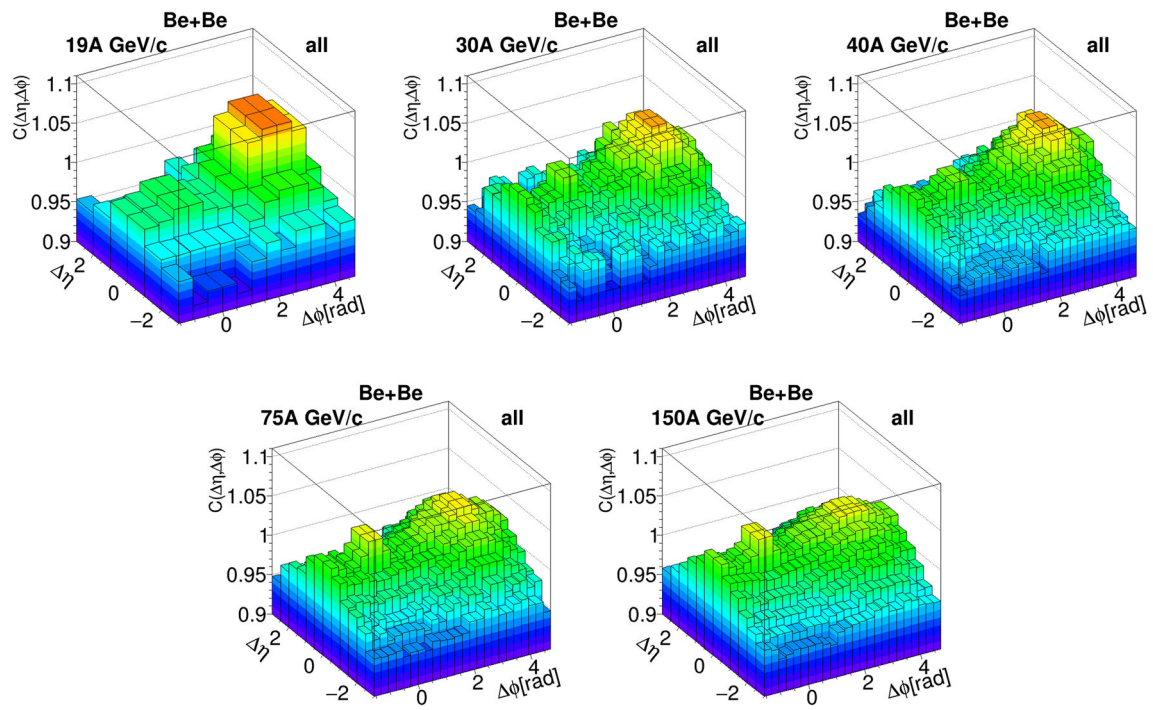
Fig. 6 Two-particle correlation function $C(\Delta\eta, \Delta\phi)$ for all charge pairs in the 5% most central Be + Be collisions at $19A$–$150A$ GeV/c
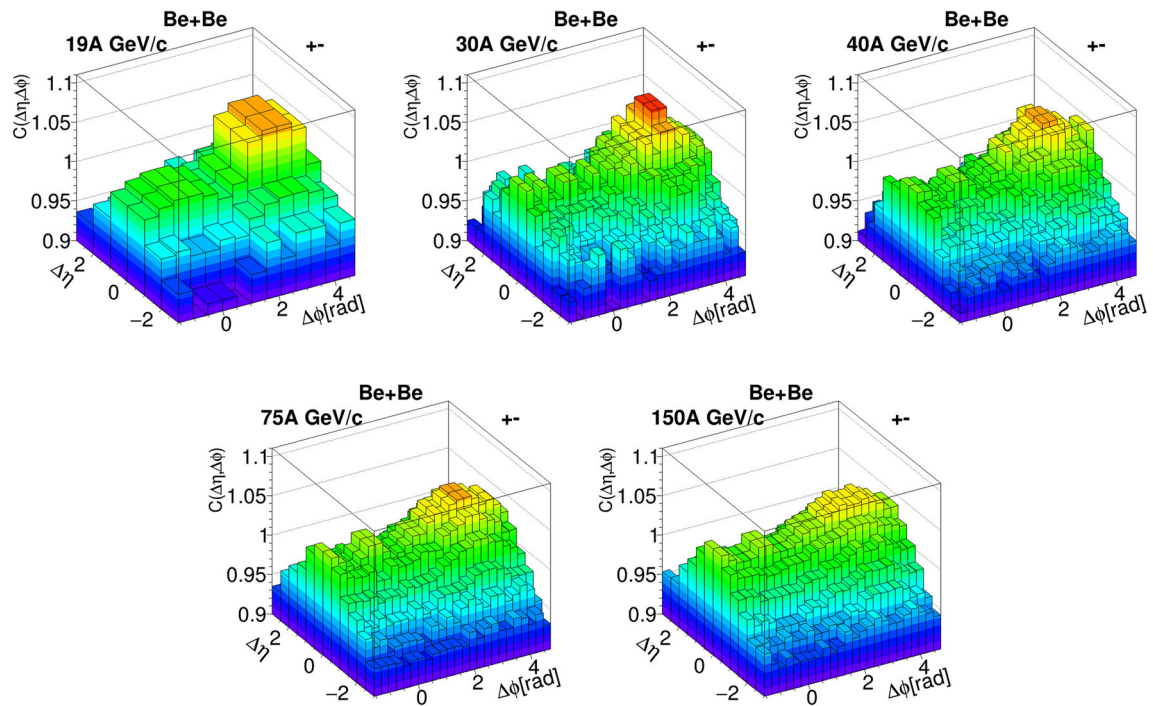

Fig. 7 Two-particle correlation function $C(\Delta\eta, \Delta\phi)$ for unlike-sign pairs in the 5% most central Be + Be collisions at $19A$–$150A$ GeV/c
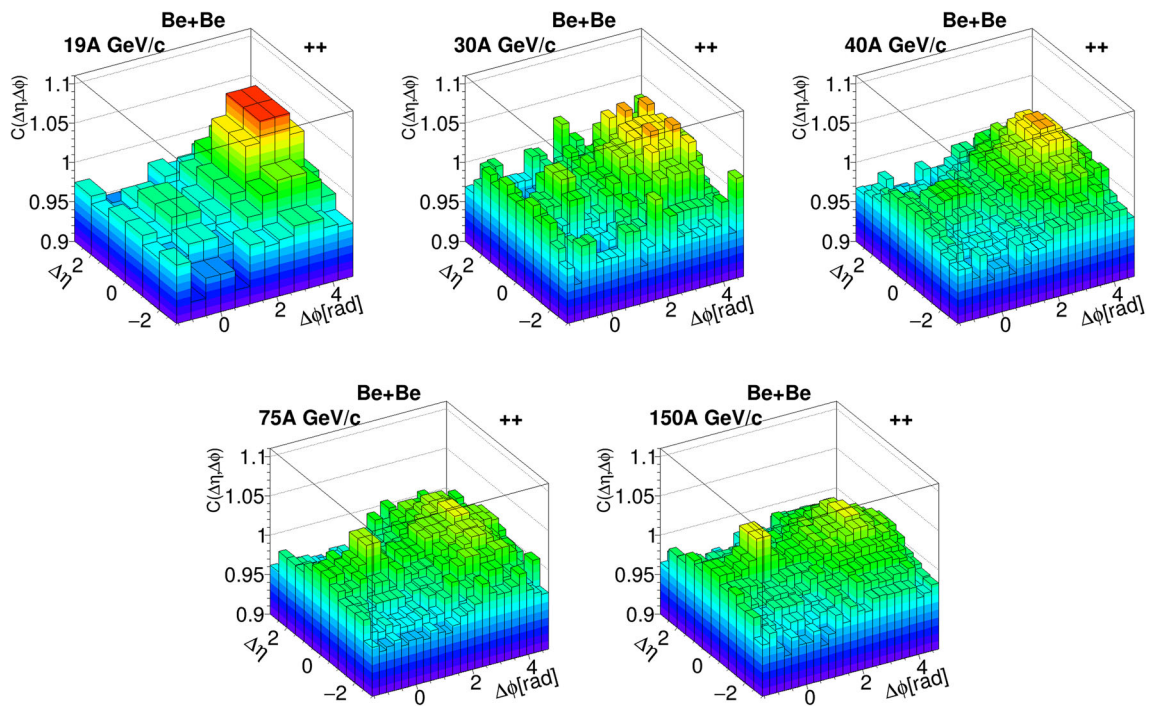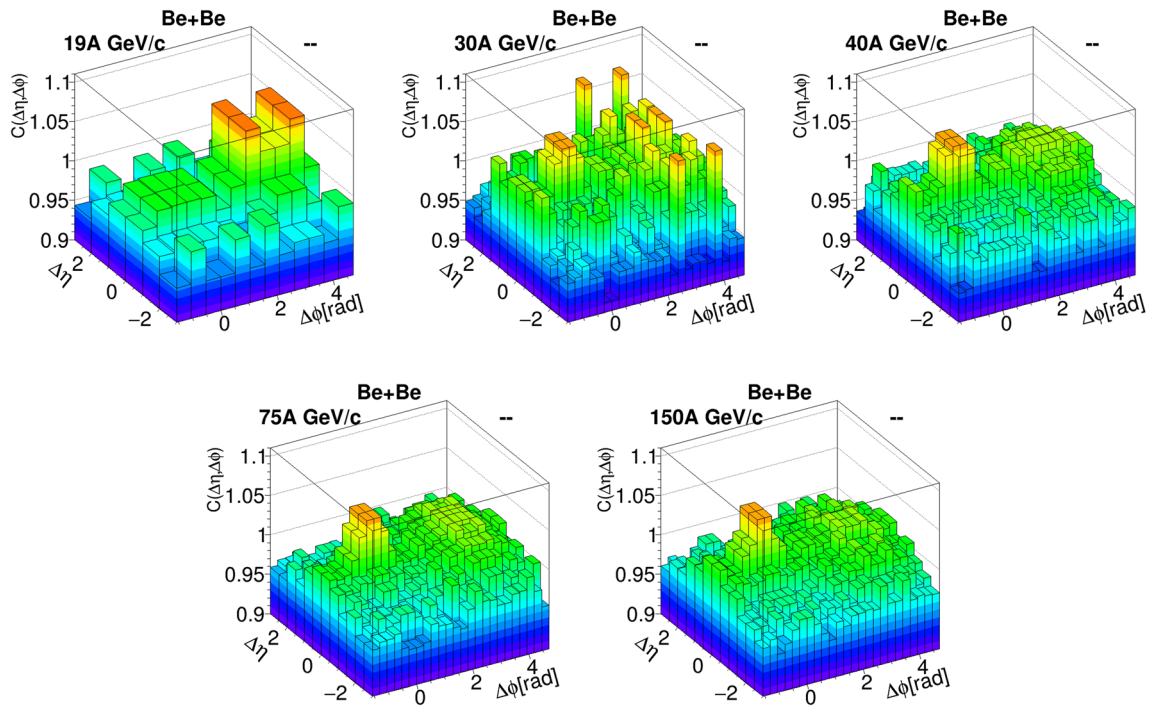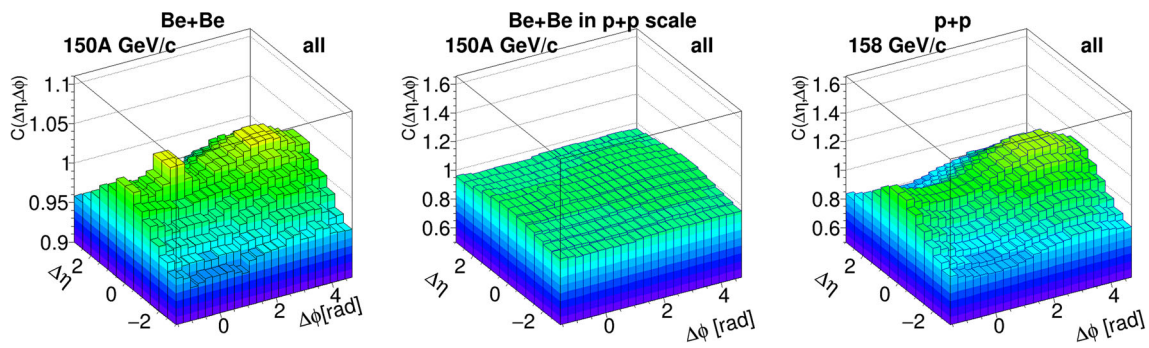
Fig. 8 Two-particle correlation function $C(\Delta\eta, \Delta\phi)$ for positive charge pairs in the 5% most central Be + Be collisions at $19A$–$150A$ GeV/c

Fig. 9 Two-particle correlation function $C(\Delta\eta, \Delta\phi)$ for negative charge pairs in the 5% most central Be + Be collisions at $19A$–$150A$ GeV/c

Fig. 10 Comparison of correlation functions $C(\Delta\phi)$ for the 5% most central Be + Be collisions and inelastic p + p interactions. Left column shows the correlation function for all charge pairs in Be + Be collisions at beam momentum 150A GeV/c per nucleon. Middle column: the same Be + Be correlation function, but shown in the vertical scale used for p + p interactions. Right column: p + p correlation function for all pairs at beam momentum 158 GeV/c taken from Ref. [9]

for beryllium–beryllium collisions (left panel) with results from proton–proton interactions (right panel). The most striking feature is the general difference in correlation strength. Due to the larger combinatorical background, the correlation strength is diluted in Be + Be collisions. For better comparison of the strengths the center panel of Fig. 10 presents the Be + Be results at the p + p scale. The dilution amounts to approximately a factor of 5 which is close to the ratio of pion multiplicities produced in Be + Be and p + p collisions. This is expected in simple models where e.g. the resonance to direct pion production ratio is assumed to be the same in both reactions.

7.1.1 The near-side correlations behaviour

While both in Be + Be collisions and p + p interactions the away side hill is qualitatively similar, a visible difference of the structure at $C(\Delta\phi)$ can be seen. To visualize this, the ratio of the difference of the correlation functions from unity for Be + Be ($C^{\mathrm{BeBe}} - 1$) and p + p ($C^{\mathrm{pp}}/5 - 1$) was calculated for all pair combinations and beam momenta using the following formula:

$$R_{\mathrm{pp}}^{\mathrm{BeBe}} = \frac{C^{\mathrm{BeBe}} - 1}{C^{\mathrm{pp}}/5 - 1}. \tag{4}$$

The results for all pair combinations and beam momenta are shown in Fig. 11. The near-side peak structure clearly increases in height with beam momentum, demonstrating that the contribution to that region in Be + Be is stronger than in p + p reactions.

The correlation functions $C - 1$ for both colliding systems is presented in Fig. 12 in a near-side slice of $0 \leq \Delta\eta \leq 0.5$ versus $\Delta\phi$. The values of C for p + p interactions were scaled down by a factor of 5 to approximately account for the expected dilution effect.

In Sect. 6.1 the HBT + Coulomb + FS effects were pointed out as a possible source of the peak in the near-side region.

These correlations are indeed of importance for small relative four momentum and, as a consequence, for small relative transverse momentum Δp_T of the hadron pair. They can produce a maximum in Δp_T at about 20 MeV/c, stretching out to about 50 MeV/c (see e.g. Refs. [32–35]).

The relative azimuthal angle is related to the relative transverse momenta of the hadron pair via the relation:

$$\Delta p_T^2 = p_{T1}^2 + p_{T2}^2 - 2p_{T1}p_{T2}\cos(\Delta\phi) \tag{5}$$

$$\Delta\phi = \arccos\left(1 - \frac{\Delta p_T^2}{2p_T^2}\right). \tag{6}$$

For $\Delta p_T = 0.05$ GeV/c and the most probable value of transverse momenta of about 0.4 GeV/c this corresponds to a difference in azimuthal angle $\Delta\phi$ of about 0.1 rad. Therefore HBT + Coulomb + FS correlations can explain only a fraction of the enhancement in the first $\Delta\phi$ bin in the panels of Fig. 12. A similar conclusion was drawn e.g. in Refs. [36,37] at RHIC and LHC energies in nucleus–nucleus and p + A interactions. There a cut on $\Delta\phi$ was applied to remove HBT + C + FS effects in order to allow cleaner studies of processes like mini-jet production.

In the Fig. 12 we observe larger near-side correlations for negative charge than for positive charge pairs. However, one should remember that the total number of negative charge pairs is about 2–3 times smaller than that of the positive charge pairs. This is expected, because of the proton admixture in the positive charge pair sample and, in consequence, contributions of pp and $p\pi^+$ pairs in addition to $\pi^+\pi^+$ combinations. It is not clear, however, why the contribution to the correlation peak from negative charge pairs ($\Delta\phi < 7.5°$) seems to be smaller ($\approx 10 \pm 2\%$) than that from positive charge pairs ($\approx 20 \pm 2\%$). We hope to understand better the observed difference with the larger statistics data from Ar + Sc collisions.

Due to limited statistics, in particular for 19A and 30A GeV/c, rather large bins in $\Delta\phi$ were used in our analysis.
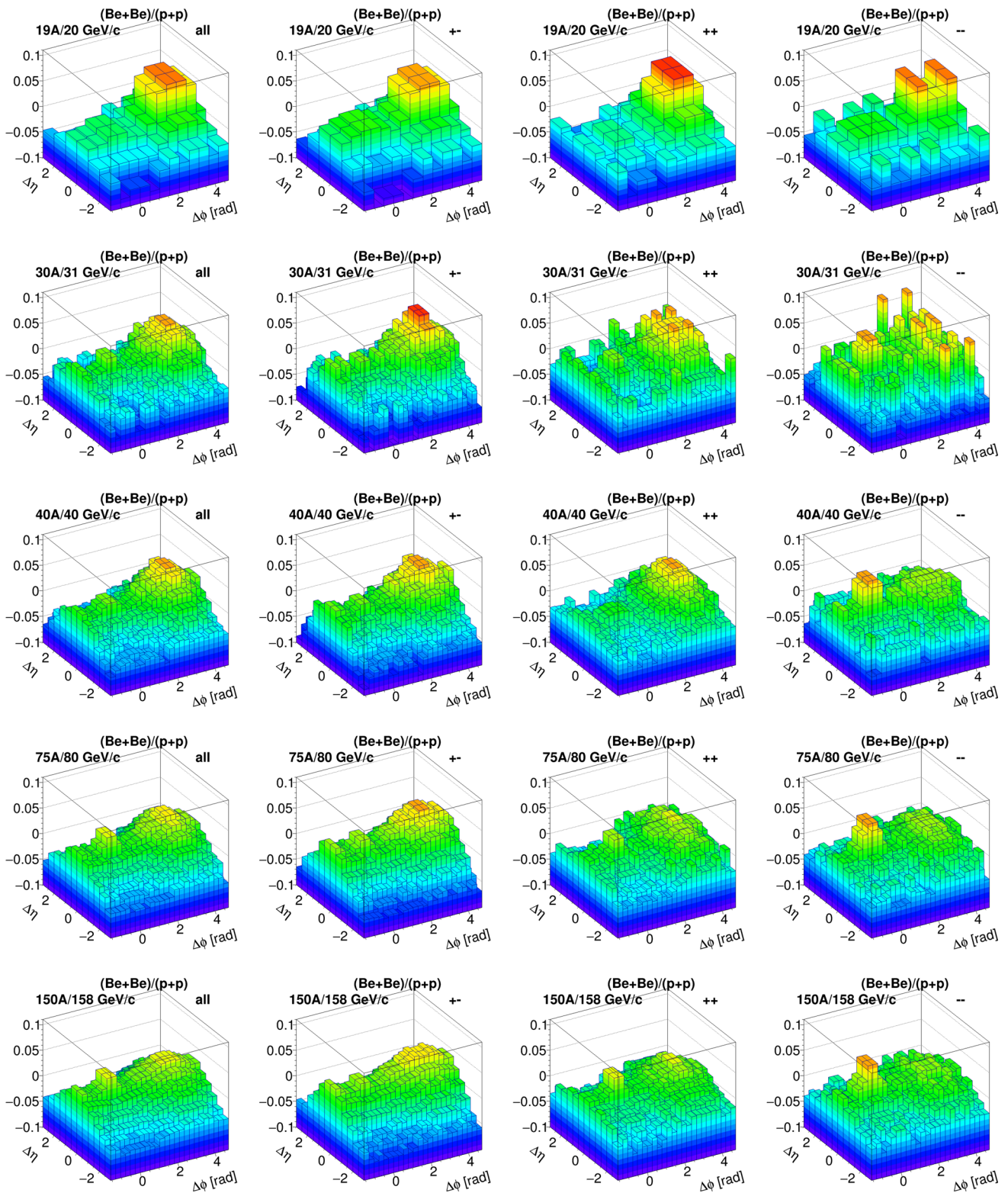
Fig. 11 Ratio R_{pp}^{BeBe} for all pair combinations and momenta (following formula Eq. 4). Each row shows different beam momentum (beam momentum increases downwards). Every column presents results for different pair combinations (from left to right: all pairs, unlike-sign pairs, positive pairs, negative pairs). Note that correlation function for p + p was scaled down by a factor of 5 before calculation of ratio
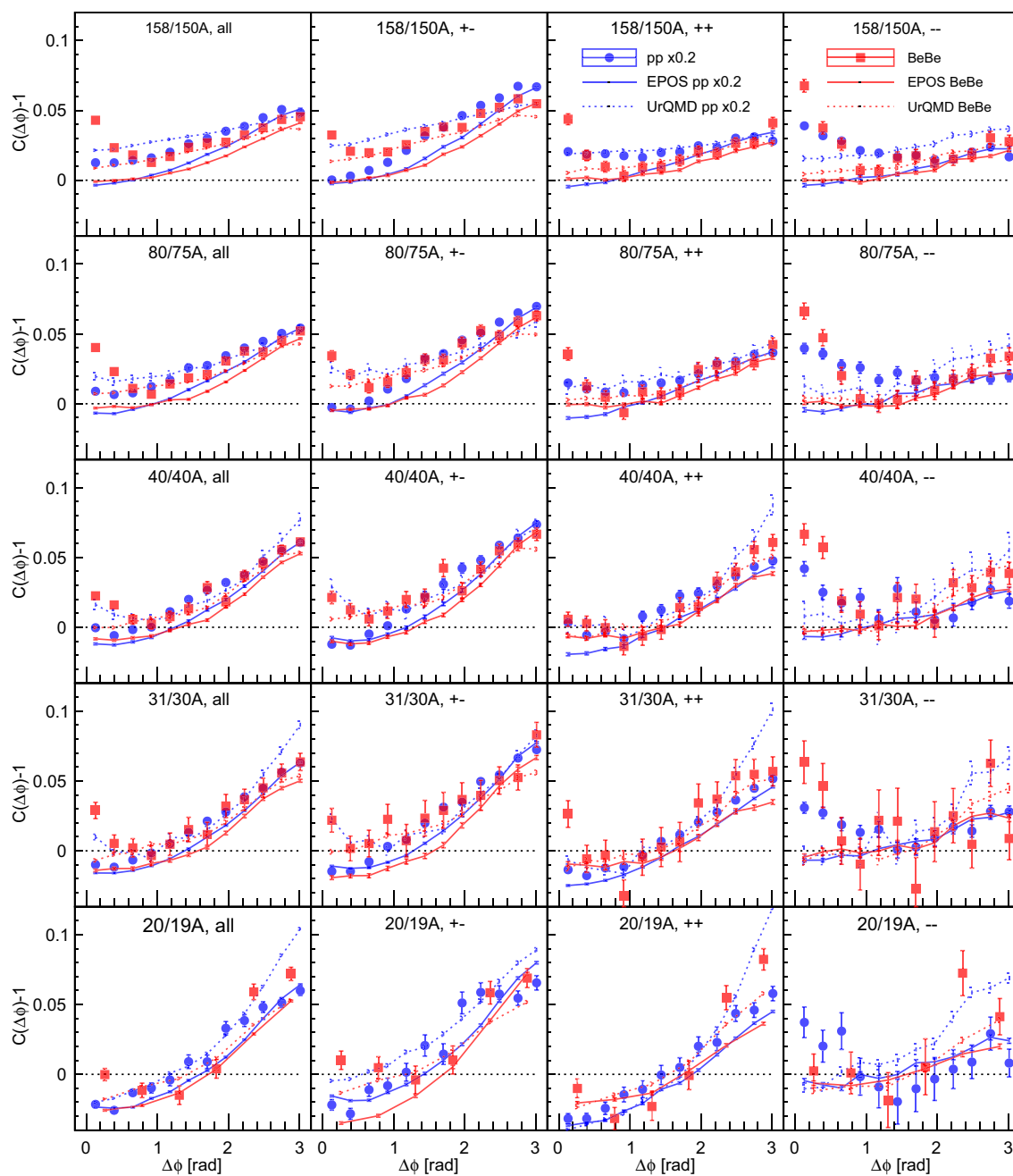
Fig. 12 Comparison of two-particle correlation function $C - 1$ for the range $\Delta\eta \in [0, 0.5)$ in collisions of p + p (blue) and Be + Be (red). Columns from left to right show results for: all charge pairs, unlike-sign pairs, positive pairs, and negative pairs. Results for different beam momenta are plotted in successive rows. Data results are shown by markers (circles for p + p and squares for Be + Be), model results by lines (solid lines show EPOS while dotted lines – UrQMD results). The results for p + p interactions were additionally scaled down by a factor of 5. Only statistical uncertainties are shown

To show better the influence of the HBT + Coulomb + FS mechanisms the results of Fig. 12 are shown in Fig. 13 with finer binning (the width of $\Delta\phi$ bin here is $3.75° \approx 0.07$ rad). This figure presents the region of $\Delta\phi$ up to 1 radian for beam momenta of $40A$, $75A$, and $150A$ GeV/c. One finds that the fraction of the two first bins corresponds to $(10.5 \pm 1.5)\%$, $(15.6\pm2.0)\%$ and $(16.6\pm2.0)\%$ of the whole near-side effect for $40A$, $75A$, and $150A$ GeV/c respectively, for the sum of all charge configurations. This excludes the dominant role of the HBT + Coulomb + FS mechanisms in the near-side region.
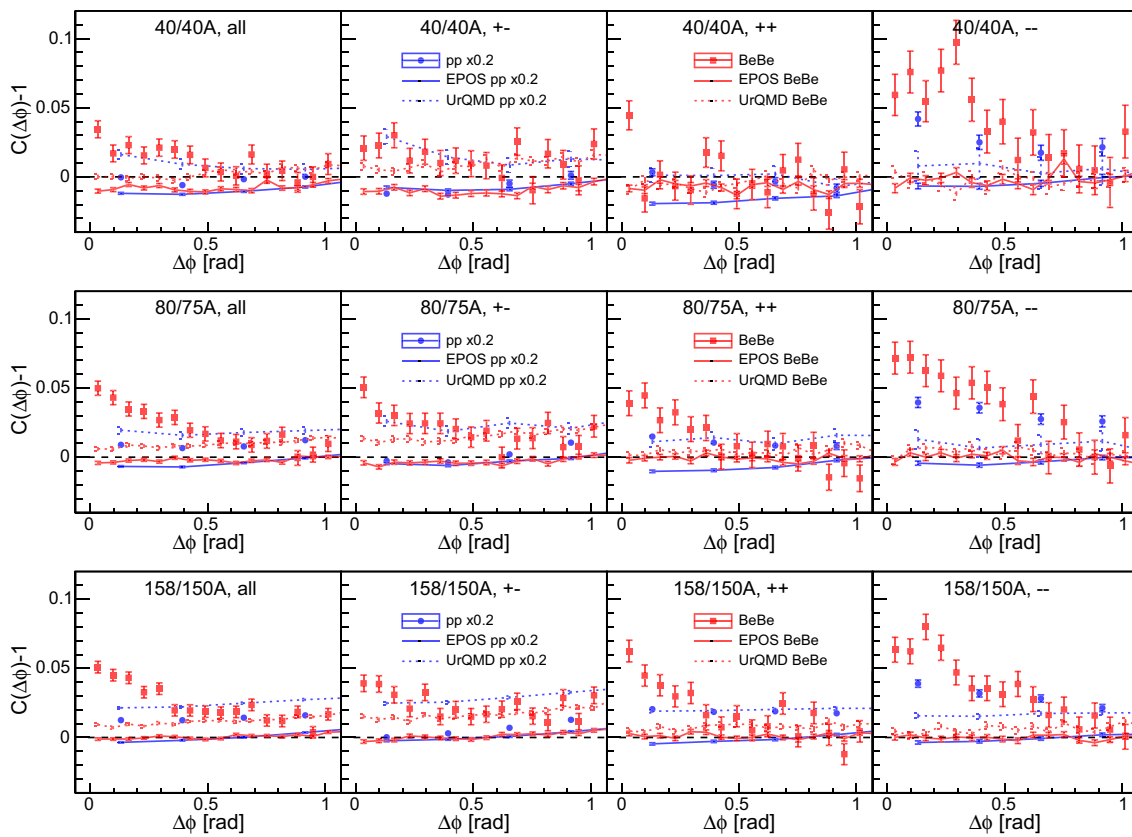
Fig. 13 Comparison of two-particle correlation function $C - 1$ for the range $\Delta\eta \in [0, 0.5]$ and for zoomed in range of $0 \leq \Delta\phi \leq 1$ radians. Results of collisions of p + p are marked in blue and of Be + Be are marked in red. Columns from left to right show results for: all charge pairs, unlike-sign pairs, positive pairs, and negative pairs. Results for beam momenta $40A$, $75A$, and $150A$ GeV/c are plotted in successive rows. Data results are shown by markers (circles for p + p and squares for Be + Be), model results by lines (solid lines show Epos while dotted lines – UrQMD results). The results for p + p interactions were additionally scaled down by a factor of 5. Only statistical uncertainties are shown

To better visualise the energy dependence of the near-side correlations the first three points from the Fig. 12 were summed up for different charge configurations of the hadron pairs. The result is shown in Fig. 14 for all charge and unlike-sign pairs. A strong energy dependence is observed between $19A$–$30A$–$40A$ GeV/c and $75A$–$150A$ GeV/c which could favour the onset of mini-jet formation. If the mini-jet hypothesis is correct, the correlation for oppositely charged particles may be due to local charge conservation.

In Fig. 15 the energy dependence of that sum of $C - 1$ in Be + Be collisions for the data and models is presented for different charge configurations. In the same figure the experimental results for proton–proton collisions divided by a factor of 5 (i.e. $C/5 - 1$) are plotted.

7.2 Comparison with models

Since hard-scattering processes are not expected to contribute substantially to particle production at SPS energies comparison of data with models designed to work also at low colli-
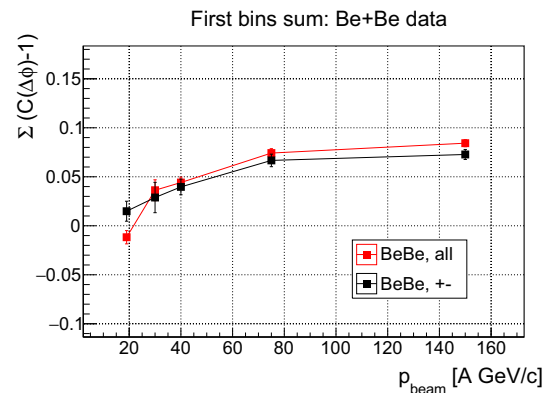
Fig. 14 The sum of two-particle correlation function $C(\Delta\eta, \Delta\phi)$ in the $\Delta\phi$ region $[0, \pi/2]$ and $\Delta\eta \in [0, 0.5]$ for unlike-charge pairs (black squares) and all charge pairs (red circles) for the 5% most central Be + Be collisions

sion energies, such as Epos and UrQMD, appear to be most appropriate. One needs to point out that unfortunately the
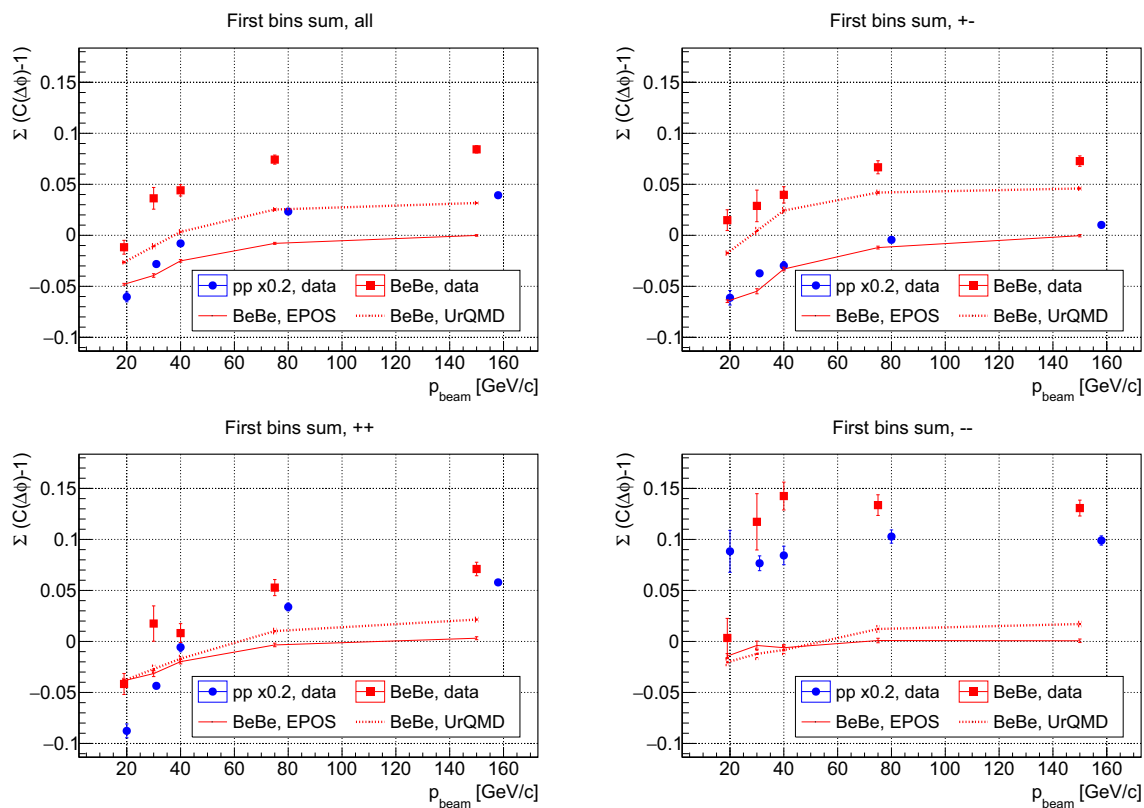
Fig. 15 The sum of two-particle correlation function $C(\Delta\eta, \Delta\phi)$ in the $\Delta\phi$ region $[0, \pi/2)$ and $\Delta\eta \in [0, 0.5)$ for different charge combinations. Top left picture for all charge pairs, top right for unlike-sign, bottom left for positive charged pairs, bottom right for negative charged.

Results for Be + Be (red squares) were compared with p + p (blue circles) and with model predictions of the corresponding charge combination. The results of p + p are scaled down by factor of 5

models do not incorporate HBT + Coulomb + FS effects. Correlations in UrQMD and EPOS are probably dominated by resonance production and string fragmentation processes. The resonance contribution was taken into account in both UrQMD and EPOS models, but discrepancies between data and simulations persist (see discussion below).

Although SPS energies are rather low, other models, which take into account the possibility of quark-gluon phase formation, were also proposed to explain the observed near-side correlations. These were interpreted as a result of jet fragmentation or color-tube fragmentation [38,39], originating from a Glasma flux tube [40] or from Parton Bubbles [16,17,41]. The latter were initially proposed by Van Hove [18].

7.3 Comparison with the EPOS and UrQMD models

The final corrected results on $C(\Delta\eta, \Delta\phi)$ were compared with predictions of the pure (i.e. not reconstructed) EPOS and UrQMD models. They are presented in the form of projections on the $\Delta\eta$ and $\Delta\phi$ axes in Figs. 16 and 17, respectively. In case of projection onto the $\Delta\eta$ axis the correlations

were divided into four sub-ranges of $\Delta\phi$: $0 \leq \Delta\phi < \frac{\pi}{4}$, $\frac{\pi}{4} \leq \Delta\phi < \frac{\pi}{2}$, $\frac{\pi}{2} \leq \Delta\phi < \frac{3\pi}{4}$, and $\frac{3\pi}{4} \leq \Delta\phi < \pi$. In case of projection onto the $\Delta\phi$ axis, the $\Delta\eta$ axis was divided into three sub-ranges: $0 \leq \Delta\eta < 1$, $1 \leq \Delta\eta < 2$, and $2 \leq \Delta\eta < 3$. The functions

$$C(\Delta\eta) = \frac{N_{\text{mixed}}^{\text{pairs}}}{N_{\text{data}}^{\text{pairs}}} \frac{D(\Delta\eta)}{M(\Delta\eta)} \qquad (7)$$

and

$$C(\Delta\phi) = \frac{N_{\text{mixed}}^{\text{pairs}}}{N_{\text{data}}^{\text{pairs}}} \frac{D(\Delta\phi)}{M(\Delta\phi)} \qquad (8)$$

were recalculated in those sub-ranges. Full statistical uncertainty analysis was performed in each sub-range as well. In case of systematic uncertainty analysis, the general method of calculation was similar to the one mentioned in Sect. 5.5, however here the mean systematic uncertainty was not calculated. The difference of (loose–tight) was shown in each bin separately instead. In order to present the results in a clear way, only two sub-ranges are shown in Figs. 16 and 17.
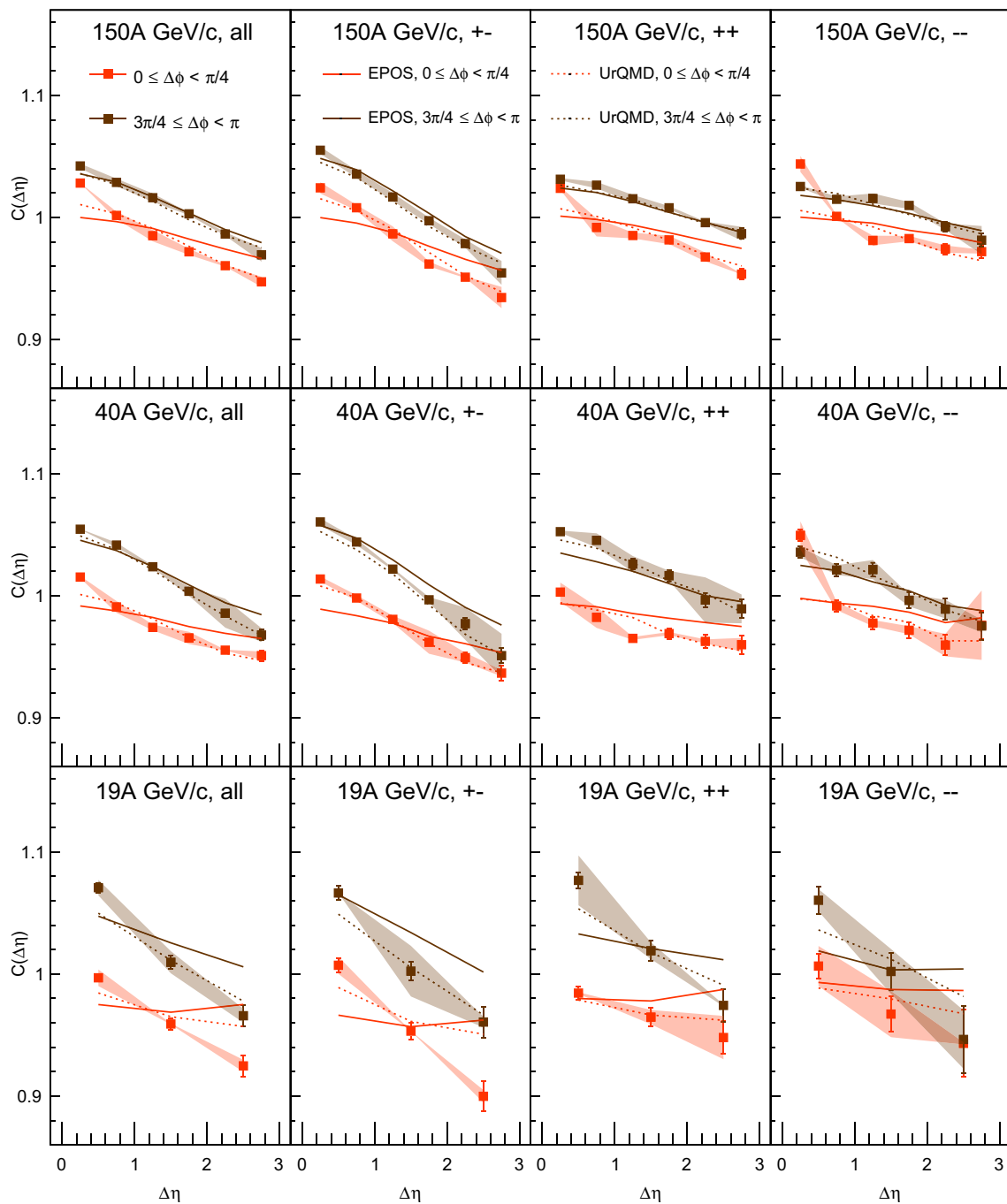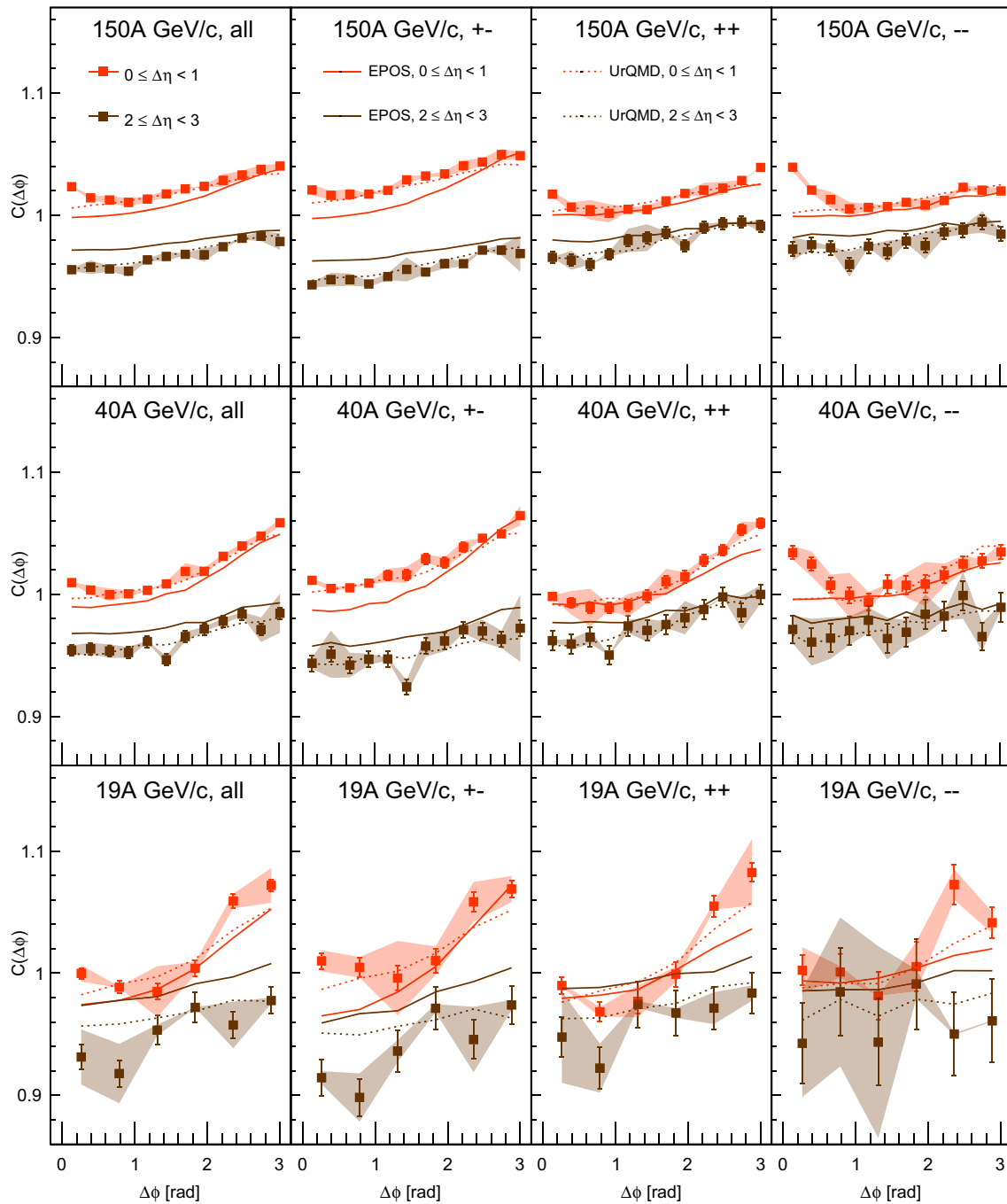
Fig. 16 Two-particle correlation function $C(\Delta\eta)$ obtained from projection of $C(\Delta\eta, \Delta\phi)$ onto the $\Delta\eta$ axis for subranges of $\Delta\phi$. From left to right the columns show respectively: all charge pairs, unlike-sign pairs, positive charge pairs, and negative charge pairs. Vertical bars denote statistical and shaded regions denote systematic uncertainties. Predictions of the Epos model are shown by solid curves and the UrQMD model by dotted curves. Legend applies to all panels

The UrQMD model predictions are in reasonable agreement with the measured data for both $40A$ and $150A$ GeV/c (dashed lines in Figs. 16 and 17) for all charge combinations. However some differences are seen in the region of the smallest $\Delta\phi$ and $\Delta\eta$ points. The Epos model works well for away-side correlations (large $\Delta\eta$ and $\Delta\phi$) and fails in the near-side region (full lines in Figs. 16 and 17). At the smallest beam momentum $19A$ GeV/c, the deviations between data and both models are quite large, but the statistical uncertainties are large and the models are not intended for this low energy.

Fig. 17 Two-particle correlation function $C(\Delta\phi)$ obtained from projection of $C(\Delta\eta, \Delta\phi)$ onto the $\Delta\phi$ axis for subranges of $\Delta\eta$. From left to right the columns show respectively: all charge pairs, unlike-sign pairs, positive charge pairs, and negative charge pairs. Vertical bars denote statistical and shaded regions denote systematic uncertainties. Predictions of the EPOS model are shown by solid curves and the UrQMD model by dotted curves. Legend applies to all panels

Such a discrepancy between both models predictions and the data exists as well for the region $\Delta\eta < 0.5$, $\Delta\phi < \pi/2$ as evident from Fig.12. It appears for both Be + Be and p + p interactions and different charge combinations.

The comparison between model predictions and the Be + Be data in the region of small $\Delta\eta$ and $\Delta\phi < \pi/2$ is shown in Fig. 15. Both models underpredict the correlation strength for all the energies measured, but the discrepancy is significantly larger for Epos predictions.

8 Summary

The $C(\Delta\eta, \Delta\phi)$ correlation function was studied by the NA61/SHINE experiment in the 0–5% most central Be + Be collisions for a range of different incident beam momenta: $19A$, $30A$, $40A$, $75A$, and $150A$ GeV . Near-side and away-side correlations were observed and measured as a function of incident momentum and particle charge combinations. The strength of the correlation was compared with that observed by NA61/SHINE in p + p [9] interactions for which the same experimental conditions were applied. A strong suppression of the correlation function is observed as compared with p + p interaction.

In Be + Be interactions, one observes a back-to-back correlation which is rather wide in $\Delta\phi$ and decreases with energy (see Figs. 16, 17). The correlation function behaviour of the data is qualitatively described by the UrQMD 3.4 and Epos 1.99 models. The UrQMD model shows better quantitative agreement.

A narrow enhancement around $(\Delta\eta, \Delta\phi) = (0, 0)$ appears clearly for Be + Be collisions (see Figs. 12, 17). It is wider (RMS about $25° \approx 0.45$ rad) in $\Delta\phi$ than expected from the contribution of HBT + Coulomb + FS correlations alone and increases with incident energy (see Fig. 14). This observation disagrees with predictions of the studied models, which do not include quantum statistics and Coulomb repulsion effects, but simulate only the production of the majority of hadron resonances. Much stronger near-side correlations were observed at higher energies in nucleus–nucleus and p + A interactions [36,37]. The NA61/SHINE experiment continues correlation studies in $\Delta\eta$, $\Delta\phi$ for Ar + Sc and Xe + La collisions. The results for different nucleus sizes may help to obtain more insight into the importance of the proposed mechanisms.

References

1. N. Abgrall et al. (NA61/SHINE Collaboration), JINST **9**, P06005 (2014). https://doi.org/10.1088/1748-0221/9/06/P06005
2. M. Gaździcki, P. Seyboth, Acta Phys. Polon. B **47**, 1201 (2016). https://doi.org/10.5506/APhysPolB.47.1201
3. K. Eggert et al., Nucl. Phys. B **86**, 201 (1975). https://doi.org/10.1016/0550-3213(75)90440-X
4. B. Alver et al. (PHOBOS Collaboration), Phys. Rev. C **75**, 054913 (2007). https://doi.org/10.1103/PhysRevC.75.054913
5. R.J. Porter, T.A. Trainor (STAR Collaboration), Acta Phys. Polon. B **36**, 353 (2005)
6. R.J. Porter, T.A. Trainor, Soft and hard components of two-particle distributions on (y(t), eta, phi from p-p collisions at s**(1/2) = 200-GeV. in *Ultra-relativistic nucleus-nucleus collisions. Proceedings, 17th International Conference, Quark Matter 2004, Oakland, USA, January 11–17, 2004* (2004)

7. B. Abelev et al. (ALICE Collaboration), Phys. Lett. B **741**, 38–50 (2015). https://doi.org/10.1016/j.physletb.2014.11.028

8. B. Alver et al. (PHOBOS Collaboration), Phys. Rev. C **81**, 024904 (2010). https://doi.org/10.1103/PhysRevC.81.024904

9. A. Aduszkiewicz et al. (NA61/SHINE Collaboration), Eur. Phys. J. C **77**(2), 59 (2017). https://doi.org/10.1140/epjc/s10052-017-4599-x

10. B. Maksiak, PhD thesis, Faculty of Physics, Warsaw University of Technology, CERN-THESIS-2016-282 (2016)

11. O. Berrig et al. (CERN and NA61/SHINE Collaboration), Technical Report, 2011. CERN-SPSC-2011-005

12. M. Gazdzicki, O. Hansen, Nucl. Phys. A **528**, 754–770 (1991). https://doi.org/10.1016/0375-9474(91)90261-4

13. J.L. Nagle, W.A. Zajc, Ann. Rev. Nucl. Part. Sci. **68**, 211–235 (2018). https://doi.org/10.1146/annurev-nucl-101916-123209

14. S. Mohapatra, EPJ Web Conf. **172**, 05002 (2018). https://doi.org/10.1051/epjconf/201817205002

15. R.S Bhalerao, Collectivity in large and small systems formed in ultrarelativistic collisions (2020)

16. S.J. Lindenbaum, R.S. Longacre, M. Kramer, Eur. Phys. J. C **30**, 241–253 (2003). https://doi.org/10.1140/epjc/s2003-01268-3

17. S.J. Lindenbaum, R.S. Longacre, Phys. Rev. C **78**, 054904 (2008). https://doi.org/10.1103/PhysRevC.78.054904

18. L. Van Hove, Z. Phys. C **27**, 135 (1985). https://doi.org/10.1007/BF01642492

19. S. Chatrchyan et al. (CMS Collaboration), Phys. Lett. B **718**, 795–814 (2013). https://doi.org/10.1016/j.physletb.2012.11.025

20. V. Khachatryan et al. (CMS Collaboration), Phys. Rev. Lett. **116**(17), 172302 (2016). https://doi.org/10.1103/PhysRevLett.116.172302

21. Particle Population Matrix definitions. https://edms.cern.ch/document/1700774/1

22. D. Banas et al., Eur. Phys. J. Plus **134**(1), 44 (2019). https://doi.org/10.1140/epjp/i2019-12465-9

23. PSD acceptance maps for event selection. https://edms.cern.ch/document/1867336/1

24. N. Abgrall et al. (NA61/SHINE Collaboration), Technical Report. CERN-SPSC-2014-031, SPSC-SR-145, CERN, Geneva (2014)

25. K. Werner, F.-M. Liu, T. Pierog, Phys. Rev. C **74**, 044902 (2006). https://doi.org/10.1103/PhysRevC.74.044902

26. E. Kaptur (NA61/SHINE Collaboration), PoS **CPOD2014**, 053 (2015). https://doi.org/10.22323/1.217.0053

27. R. Brun et al. GEANT Detector Description and Simulation Tool (1994)

28. N. Abgrall, PhD thesis, Geneva University. CERN-THESIS-2011-165 (2011)

29. N. Abgrall et al. (NA61/SHINE Collaboration), Eur. Phys. J. C **74**, 2794 (2014). https://doi.org/10.1140/epjc/s10052-014-2794-6

30. S. Bass et al., Prog. Part. Nucl. Phys. **41**, 255–369 (1998). https://doi.org/10.1016/S0146-6410(98)00058-1

31. M. Bleicher et al., J. Phys. G **25**, 1859–1896 (1999). https://doi.org/10.1088/0954-3899/25/9/308

32. D. Kincses, M.I. Nagy, M. Csanád. Coulomb and strong interactions in the final state of HBT correlations for Lévy type source functions (2019)

33. M.A. Lisa et al., Ann. Rev. Nucl. Part. Sci. **55**, 357–402 (2005). https://doi.org/10.1146/annurev.nucl.55.090704.151533

34. L. Martin et al., Particle correlations in ultrarelativistic heavy ion experiments STAR at RHIC and ALICE at LHC, in *4th TAPS International Workshop on Electromagnetic and Hadronic Probes of Nuclear Matter*, vol. 3 (1998). https://lss.fnal.gov/archive/other/subatech-98-02.pdf

35. Y. Sinyukov et al., Phys. Lett. B **432**, 248–257 (1998). https://doi.org/10.1016/S0370-2693(98)00653-4

36. J. Adams et al. (STAR Collaboration), Phys. Rev. C **75**, 034901 (2007). https://doi.org/10.1103/PhysRevC.75.034901

37. S. Acharya et al. (ALICE Collaboration), Phys. Rev. C **100**(4), 044903 (2019). https://doi.org/10.1103/PhysRevC.100.044903

38. J. Adams et al. (STAR Collaboration), Nucl. Phys. A **757**, 102–183 (2005). https://doi.org/10.1016/j.nuclphysa.2005.03.085

39. C. Marquet, Nucl. Phys. A **855**, 158 (2011). https://doi.org/10.1016/j.nuclphysa.2011.02.033

40. A. Dumitru et al., Nucl. Phys. A **810**, 91–108 (2008). https://doi.org/10.1016/j.nuclphysa.2008.06.012

41. S.J. Lindenbaum, R.S. Longacre, J. Phys. G **26**, 937–956 (2000). https://doi.org/10.1088/0954-3899/26/6/314